A Hybrid Dynamical–Statistical Downscaling Technique. Part II: End-of-Century Warming Projections Predict a New Climate State in the Los Angeles Region

FENGPENG SUN, DANIEL B. WALTON, AND ALEX HALL

Department of Atmospheric and Oceanic Sciences, University of California, Los Angeles, Los Angeles, California

(Manuscript received 12 March 2014, in final form 4 March 2015)

ABSTRACT

Using the hybrid downscaling technique developed in part I of this study, temperature changes relative to a baseline period (1981–2000) in the greater Los Angeles region are downscaled for two future time slices: midcentury (2041–60) and end of century (2081–2100). Two representative concentration pathways (RCPs) are considered, corresponding to greenhouse gas emission reductions over coming decades (RCP2.6) and to continued twenty-first-century emissions increases (RCP8.5). All available global climate models from phase 5 of the Coupled Model Intercomparison Project (CMIP5) are downscaled to provide likelihood and uncertainty estimates. By the end of century under RCP8.5, a distinctly new regional climate state emerges: average temperatures will almost certainly be outside the interannual variability range seen in the baseline. Except for the highest elevations and a narrow swath very near the coast, land locations will likely see 60–90 additional extremely hot days per year, effectively adding a new season of extreme heat. In mountainous areas, a majority of the many baseline days with freezing nighttime temperatures will most likely not occur. According to a similarity metric that measures daily temperature variability and the climate change signal, the RCP8.5 end-of-century climate will most likely be only about 50% similar to the baseline. For midcentury under RCP2.6 and RCP8.5 and end of century under RCP2.6, these same measures also indicate a detectable though less significant climatic shift. Therefore, while measures reducing global emissions would not prevent climate change at this regional scale in the coming decades, their impact would be dramatic by the end of the twenty-first century.

1. Introduction

In Walton et al. (2015, hereinafter Part I), we described a hybrid dynamical–statistical technique for downscaling the global climate models (GCMs) from phase 5 of the Coupled Model Intercomparison Project (CMIP5) to a 2-km resolution over the greater Los Angeles region. As an example of its capabilities, we applied this technique to all available CMIP5 GCMs for the RCP8.5 anthropogenic greenhouse gas emissions scenario and projected the midcentury most likely (ensemble mean) surface air warming and uncertainties arising from multiple GCMs. Part I was a proof-of-concept study demonstrating that the hybrid dynamical–statistical technique is capable of accurately capturing both large-scale warming and the spatial gradients in warming within the region because of its complex orography and coastlines. In this study, we use the hybrid dynamical–statistical technique to make a comprehensive assessment of the effects of twenty-first-century warming in the region as a function of time period and forcing scenario.

CMIP5 provides a multimodel context for understanding global climate and climate change and also provides a range of multicentury climate responses across GCMs under multiple anthropogenic forcing scenarios (Taylor et al. 2012). The organizers of the CMIP5 archive have adopted a set of forcing scenarios known as representative concentration pathways (RCPs; Moss et al. 2008; Meinshausen et al. 2011; Taylor et al. 2012). Four RCPs have been developed: RCP2.6, RCP4.5, RCP6, and RCP8.5, corresponding to the approximate radiative forcing they would produce at the end of the twenty-first century (2.6, 4.5, 6.0, and 8.5 $W m^{-2}$, respectively). The radiative forcing from 1850 to 2100 is shown in Fig. 1a for each scenario, with the historical forcing also shown

Corresponding author address: Fengpeng Sun, 7343 Math Sciences Building, 405 Hilgard Ave., Los Angeles, CA 90095.
E-mail: sun@atmos.ucla.edu

DOI: 10.1175/JCLI-D-14-00197.1

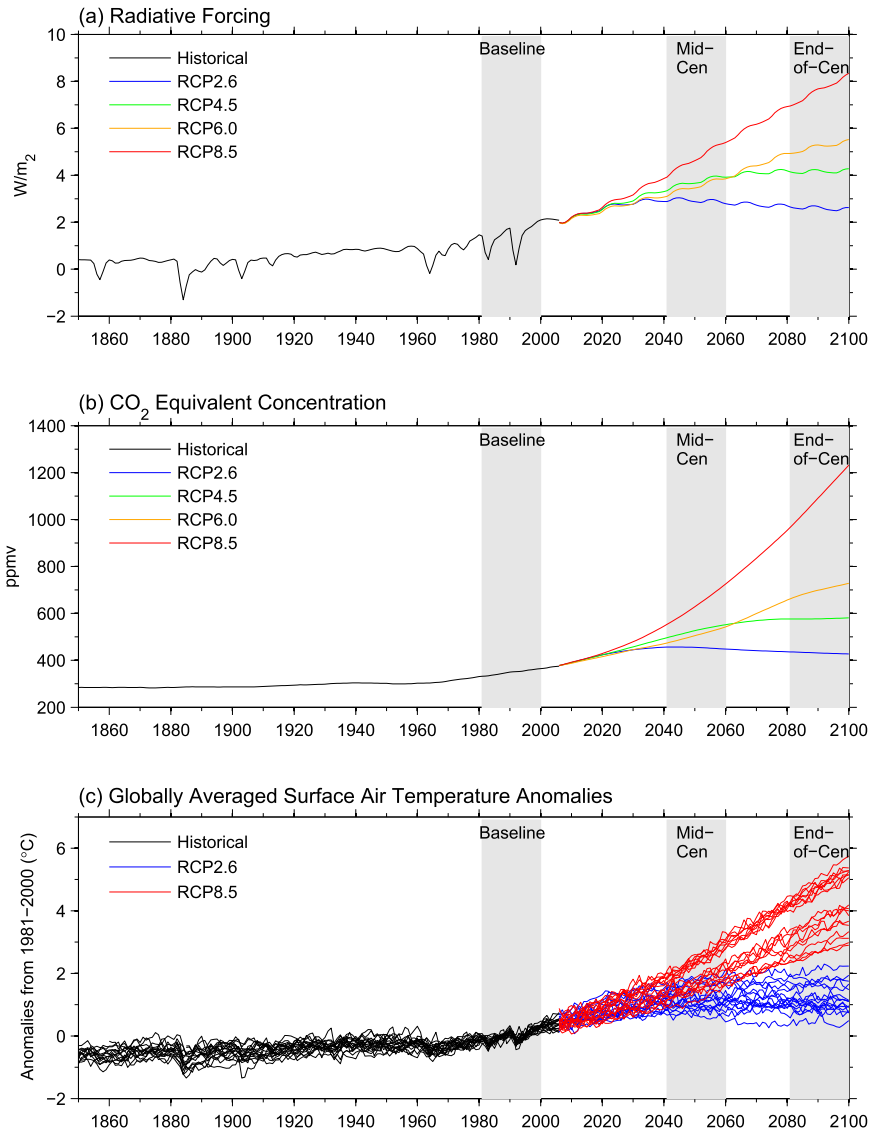

FIG. 1. (a) Total radiative forcing (anthropogenic plus natural) and (b) CO_2-equivalent concentrations for approximately the past century and four representative concentration pathways: RCP8.5, RCP6, RCP4.5, and RCP2.6 (also called RCP3-PD). (c) Global-mean surface air temperature departures from 1981–2000 mean as simulated in CMIP5 GCMs used in this study for the historical forcing (black), RCP8.5 (red), and RCP2.6 (blue). Gray shaded regions denote the baseline (1981–2000), midcentury (2041–60), and end-of-century (2081–2100) periods used in this study.

up to the year 2005. RCP2.6 is representative of a ''mitigation'' scenario, in which greenhouse gas emissions peak within the next three decades. The resulting carbon dioxide (CO_2)-equivalent concentration, encompassing the net effect of all anthropogenic forcing agents, reaches a maximum level of approximately 460 ppmv around 2050 and declines thereafter to approximately 420 ppmv by 2100 (Fig. 1b). Total radiative forcing relative to preindustrial levels peaks at about 3 W m^{-2} in the middle of the twenty-first century and declines to 2.6 W m^{-2} by 2100. In contrast to RCP2.6, RCP8.5 represents a ''business as usual'' scenario, in which greenhouse gas emissions continue to increase throughout the twenty-first century. The result is a total radiative forcing of 8.5 W m^{-2} and CO_2-equivalent concentrations greater than 1200 ppmv by 2100. Between the mitigation RCP2.6 scenario and the most aggressive business-as-usual RCP8.5 scenario are two ''stabilization'' scenarios, RCP4.5 and RCP6. In this study, however, we focus on the climate response to the two scenarios at either extreme (i.e.,

RCP8.5 and RCP2.6) to approximately sample the full range of climate outcomes associated with potential future emissions.

A sampling of the global-mean surface air temperature response to the RCP2.6 and RCP8.5 scenarios seen in the CMIP5 GCMs is shown in Fig. 1c. (Table 1 of Part I summarizes the available global climate models used in this study.) For both scenarios, there are clearly significant model-to-model differences in the warming response over the twenty-first century. For example, by 2100, for RCP2.6 scenario, surface air warming ranges from about 0.5° to 2.5°C, while for RCP8.5 scenario, the warming is about 3°–6°C. The variations in warming arise principally from differences in the GCM spatial resolutions and physical parameterizations, representing subgrid processes (e.g., cloud and the atmospheric boundary layer schemes). Thus, the various lines seen in Fig. 1c approximately represent the range of warming outcomes associated with different GCMs. For this reason, we interpret the range of outcomes as the climate change uncertainty associated with a given emissions scenario. We also interpret the average response of all the GCMs for a given emissions scenario (the ensemble mean) as the most likely outcome for that scenario. This assumes the GCMs randomly sample the true uncertainty space associated with the simulated response to anthropogenic forcing. This is the same approach to likelihood and climate change uncertainty quantification used in the Intergovernmental Panel on Climate Change (IPCC) report (Stocker et al. 2013).

In this study, we focus on three time periods: baseline (1981–2000), midcentury (2041–60), and end of century (2081–2100). These time periods are shaded in Fig. 1. Climate change is quantified by comparing midcentury and end-of-century climate states to that of the baseline. Previously, the vast majority of regional climate change studies have been performed for only 1–3 different GCMs (e.g., Hayhoe et al. 2004; Duffy et al. 2006; Déqué et al. 2007; Sato et al. 2007; Cayan et al. 2008; Salathé et al. 2010; Cabré et al. 2010). This is partly because of the computational expense of dynamically downscaling each GCM. The hybrid dynamical–statistical technique described in Part I allows us to perform downscaling of the temperature change signal for each of these future time periods and scenarios and for every available CMIP5 model.

This hybrid dynamical–statistical technique combines the ability of dynamical downscaling to capture finescale dynamics with a computationally efficient statistical model to downscale a large ensemble of GCMs. First, the Weather Research and Forecasting (WRF) Model, a regional-scale model, is used to perform two types of simulations: 1) a baseline simulation using the North American Regional Reanalysis (NARR) data as boundary and initial conditions; and 2) multiple midcentury future simulations under RCP8.5 emissions scenario by applying a previously established method (e.g., Schär et al. 1996; Hara et al. 2008; Kawase et al. 2009) to five selected GCMs, which adequately sample the range of warming amplitudes across all GCMs. In this method, initial and boundary conditions are given by adding a mean climate change signal from a given GCM to the 3-hourly NARR data. We did not downscale changes in GCM variability. Thus, any future changes in variability in the regional simulations are solely the result of WRF's dynamical response. We further discuss the caveats of this approach in section 4. Guided by an understanding of the underlying local dynamics, a simple statistical regression model is constructed relating the GCM output and the dynamically downscaled output. The statistical model consists of mathematical relationships between key aspects of the GCM warming and the warming patterns produced by dynamically downscaling. This statistical model is then used to approximate the warming patterns of the remaining GCMs, as if they had been dynamically downscaled. For more details on this hybrid approach, refer to Part I. Because we downscale the entire ensemble of GCMs, we can quantify both the ensemble-mean warming and the intermodel spread. This allows us to provide estimates of the most likely outcome and the associated uncertainty.

A robust baseline simulation (validated for surface air temperature in Part I) allows us to evaluate these climate change signals in the context of the region's substantial natural variability (Wilkinson and Rounds 1998; Abatzoglou et al. 2009). Global-mean temperatures have already increased beyond the envelope of variability (Bindoff et al. 2013). However, elevated levels of natural variability at the regional scale make this a more difficult test for regional temperatures, depending on location (Deser et al. 2012a,b, 2013; Wallace et al. 2015). This is not just an abstract statistical question. The envelope of natural variability maps out a range of physical states to which the region's inhabitants and ecosystems are already adapted. Any perturbation resulting from anthropogenic climate change therefore must be assessed against this background. Here, we present multiple analyses designed to reveal whether changes in the region's temperatures represent significant departures from the baseline state for each scenario and time slice. These include a comparison of the climate change signal to interannual variability and the region's seasonal cycle, a "similarity" metric that quantifies the degree of correspondence between the daily temperature variability of future climate and the baseline, and quantification of changes in extremely hot and cold days.

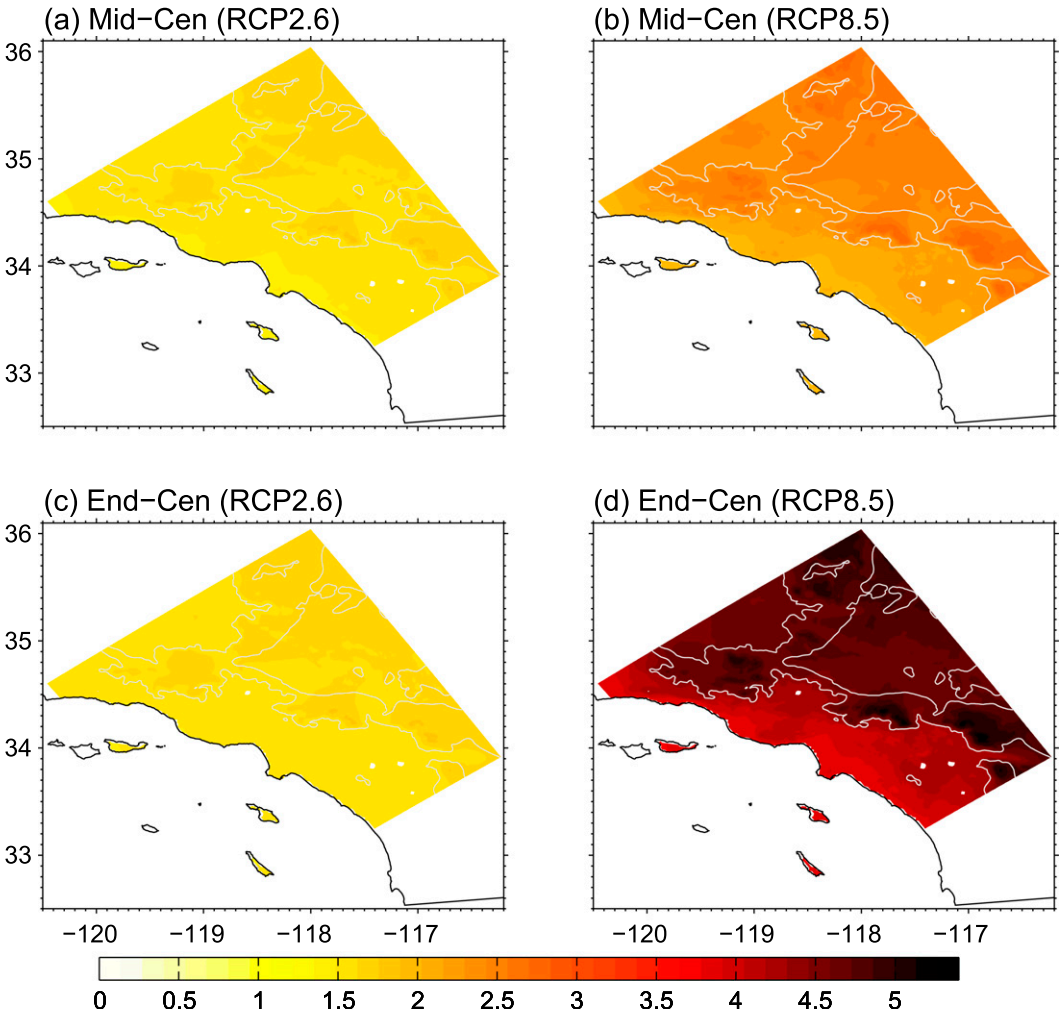

FIG. 2. Ensemble mean of downscaled annual-mean surface warming (°C) for (a) midcentury (2041–60) under RCP2.6, (b) midcentury under RCP8.5, (c) end of century (2081–2100) under RCP2.6, and (d) end of century under RCP8.5. White contours are plotted at 1000-m elevation.

Such definitive assessments of most likely outcomes and uncertainty estimates against the background of natural variability allow us to address how choices relating to greenhouse gas emissions affect climate outcomes at the regional scale and when these outcomes will emerge. This information is a foundation for efforts to adapt to climate change and also reveals the climate benefits of mitigation strategies.

The paper is organized as follows. The surface air warming comparison for multiple time periods and scenarios is shown in section 2, followed by analyses of these changes relative to the baseline seasonal cycle and interannual variability. Changes in temperature distribution and temperature extremes are assessed in section 3. In section 4, we summarize the major findings and discuss the caveats and limitations of this hybrid dynamical–statistical downscaling approach and the implications for interpreting the downscaled changes.

2. Changes in mean temperature

a. Ensemble-mean change and spread

First, we examine the annual-mean, ensemble-mean surface air warming (Fig. 2). In each scenario and time slice, the coastal areas warm less than inland areas, with the mountain peaks warming the most. These differences are most pronounced in RCP8.5. As discussed in Part I, spatial variations in the warming are due to 1) generally lower warming over the ocean in response to increasing greenhouse gases because of the ocean's relatively larger effective heat capacity and the more

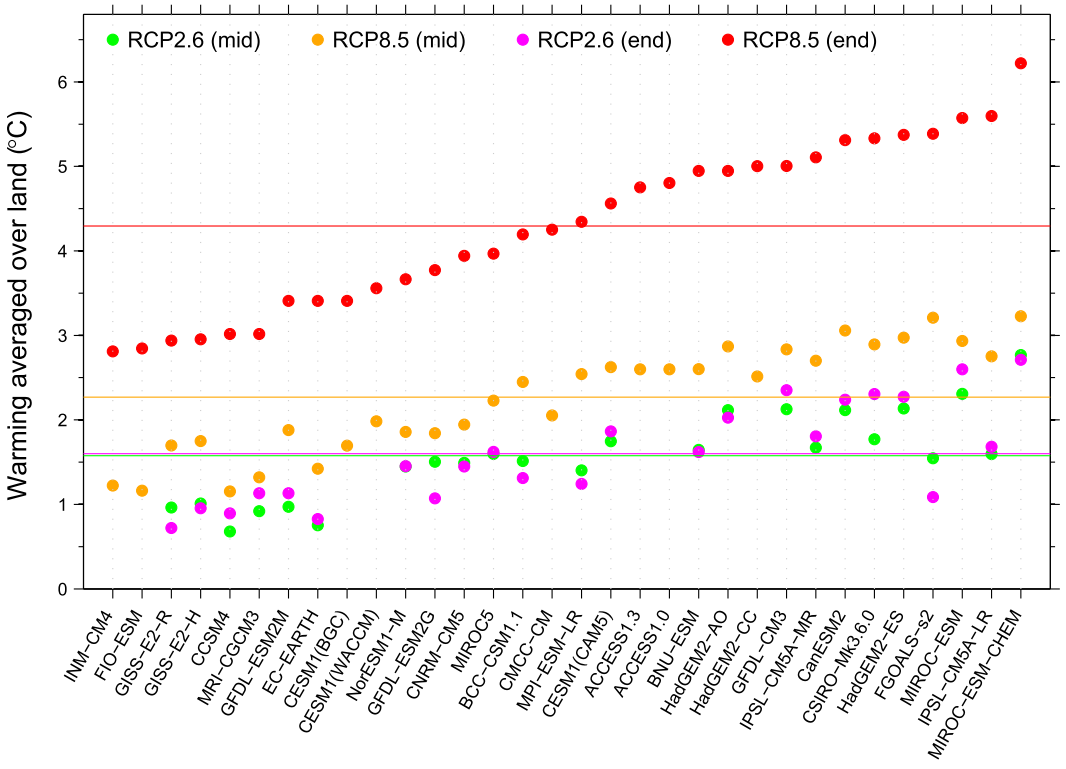

FIG. 3. Land-averaged annual-mean surface warming (°C) downscaled from each GCM for midcentury (2041–60) under RCP2.6 (green dots), midcentury under RCP8.5 (orange dots), end of century (2081–2100) under RCP2.6 (magenta dots), and end of century under RCP8.5 (red dots). Horizontal lines denote the corresponding ensemble mean across all GCMs for each scenario. (Expanded GCM names can be found online at http://www.ametsoc.org/PubsAcronymList.)

efficient ventilation of the ocean surface through latent heat fluxes, which allows enhanced downward infrared radiation in the warmer climate to be balanced with a smaller surface temperature increase over the ocean compared to land; and 2) the land–sea breeze circulation, which introduces a marine influence in the coastal zone, in this case bringing the milder warming of the ocean to the coastal zone. The annual-mean warming is highest in mountain areas mainly because they experience strong snow–albedo feedback, which is strongest in the spring months.

As shown in Figs. 2a,b and Fig. 3, the emissions scenario has only a relatively small influence on the warming at midcentury. The midcentury warming under RCP2.6 is 70% of the warming under RCP8.5. By the end of century, however, the gap between the scenarios has grown much larger. Under RCP2.6, end-of-century warming remains almost unchanged compared with midcentury warming, whereas under RCP8.5, end-of-century warming approximately doubles compared with midcentury warming, shown in Figs. 2c,d and Fig. 3. This indicates that, although the impact of global measures to reduce greenhouse gas emissions would be modest in the coming decades, it would be significant by the time the twenty-first century draws to a close.

To examine intermodel spread, we look at the annual-mean warming for each GCM, averaged over the land areas within the region (Fig. 3). The intermodel spread scales approximately with the ensemble-mean warming, with the largest spread being associated with end-of-century RCP8.5 (red dots). In this case, the ensemble-mean warming is 4.3°C, with the model predicting the most warming (MIROC-ESM-CHEM) giving a 6.2°C increase, and the model predicting the least warming (INM-CM4.0) giving a 2.8°C increase. In contrast, under the RCP2.6 scenario, the ensemble-mean warming at end of century is 1.6°C, with a maximum of 2.7°C and a minimum of 0.8°C. Thus, by the end of the century, even the model with the least warming under RCP8.5 warms more than any model under RCP2.6, despite the large intermodel spread.

b. Comparison of change signal to interannual variability

To determine if these changes in temperature are outside the variations the region is already adapted to,

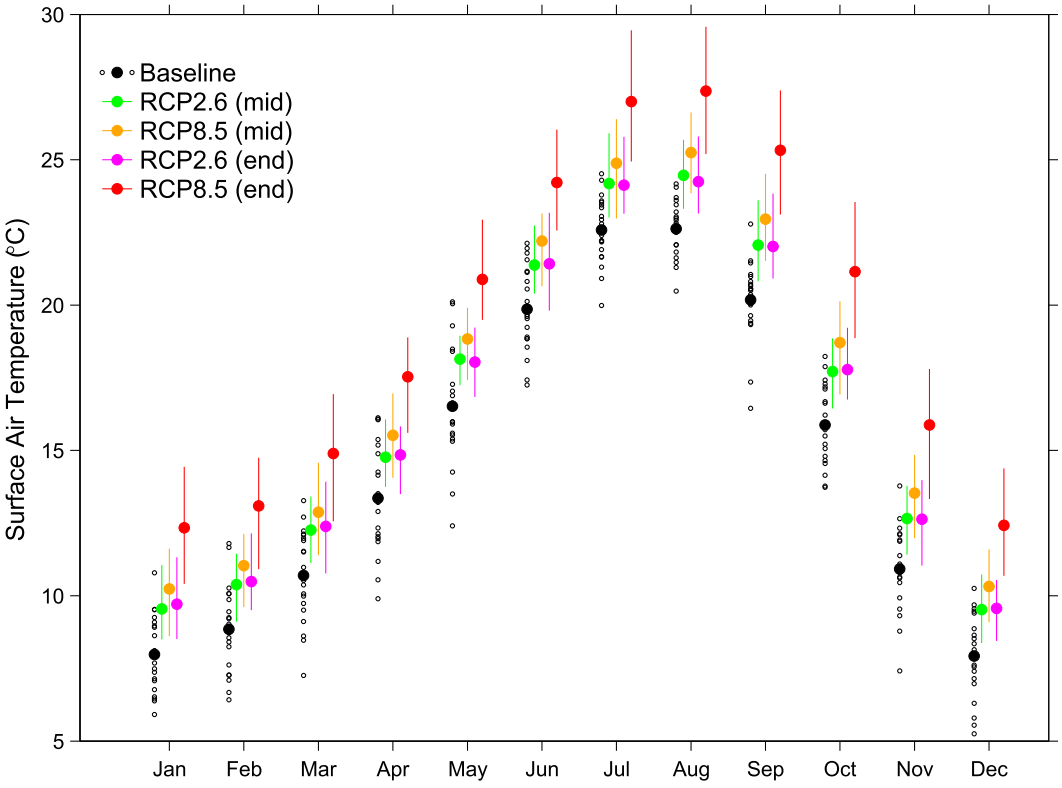

FIG. 4. Annual cycle of land-averaged surface air temperature (°C) for the baseline period (black), midcentury under RCP2.6 (green), midcentury under RCP8.5 (orange), end of century under RCP2.6 (magenta), and end of century under RCP8.5 (red). Black solid dots denote the 20-yr baseline climatology, and black open circles denote monthly mean for each year during baseline period (1981–2000). Other solid dots denote the ensemble-mean climatology for their respective scenario and time slice; bars denote the range across all the downscaled GCMs.

we compare them to the region's interannual variability. Figure 4 shows, for each month of the calendar year, the year-to-year variability in monthly mean temperatures averaged over land areas in the baseline period and the associated monthly mean warming and its intermodel spread for each future scenario and time slice. First, we note that the interannual variability for each month itself varies considerably, with the least variability occurring during the summer months, especially August, and the most variability occurring during the spring and fall months. Thus, the emergence of the climate change signal from the noise of interannual variability would be a function of time of year, even if the warming were the same for all months.

Indeed, partly because of low variability in summer, the summer warming signals are most distinct from the background variability. For example, by midcentury under RCP8.5, the most likely average future August (predicted by the ensemble mean) is warmer than the hottest August during the baseline period. Other months also show most likely future average temperatures that are outside or near the upper edge of the variability envelope for this scenario and time slice. By the end of century under RCP8.5, the ensemble-mean warming puts average temperatures well outside the baseline range for every month, even during spring, when variability is highest. Again, the effect is most dramatic in the summer months. For June, July, August, September, and October, even the model with the least warming predicts average monthly temperatures that are warmer than the hottest month within the baseline period. For the model with the most warming, the average future warm-season temperature is about 5°C greater than the warmest of the warm months in the baseline period. For the rest of the months, there is little overlap between the model spread in the average temperatures and the variability envelope. In fact, December, January, and February will be most similar to average baseline April. Future March is likely to be warmer than average baseline April; future April is likely to be warmer than average baseline May. Thus, the end-of-century warming signals under RCP8.5 represent a pronounced shift in climate compared to the baseline.

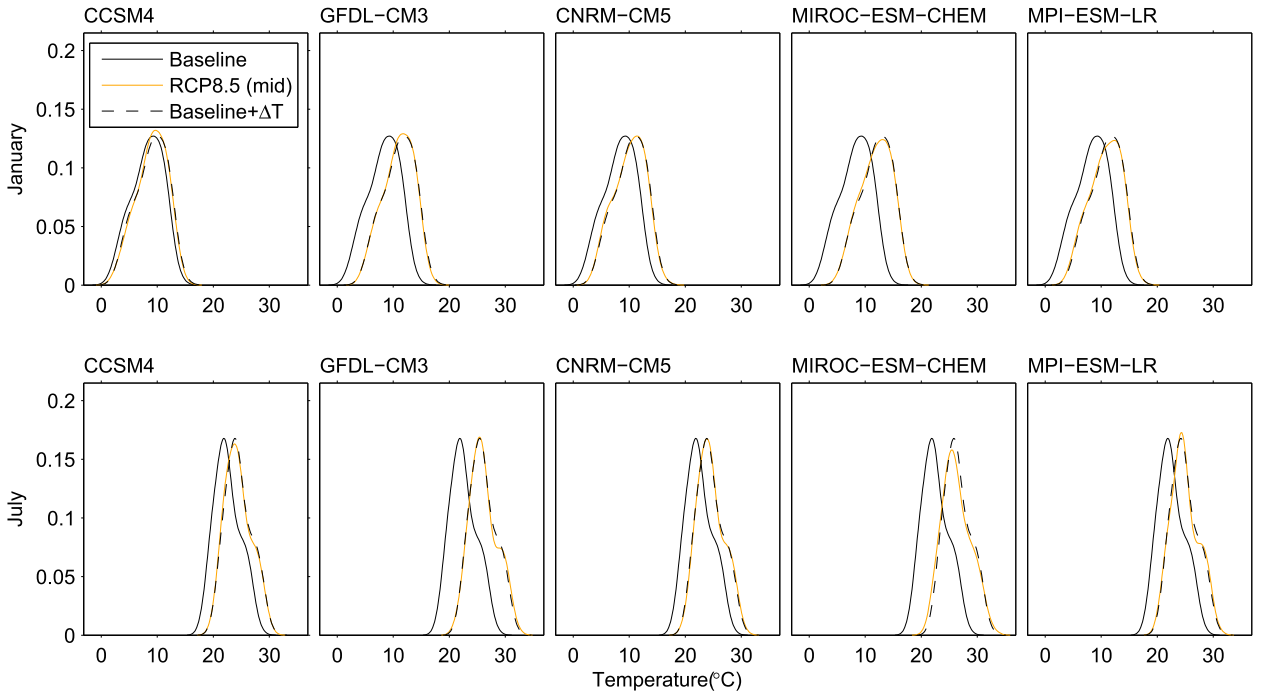

FIG. 5. PDFs of daily mean, land-averaged surface air temperature during (top) January and (bottom) July, during the baseline period (black) and at midcentury under RCP8.5 (orange) for five dynamically downscaled GCMs. The baseline distribution shifted by the statistically downscaled mean temperature change (dashed black) is shown for comparison.

Unlike the end-of-century temperatures under RCP8.5, future temperatures under RCP2.6 are mostly within the range of baseline variability for both time slices.

3. Changes in temperature distribution

In this section, we examine changes in daily temperature distribution associated with overall warmer conditions for midcentury and end-of-century time slices under RCP2.6 and RCP8.5 emissions scenarios.

The statistical model presented in Part I was designed only to calculate the change in the monthly climatological mean temperatures for each GCM in the ensemble and cannot be used directly to calculate changes in temperature distribution. However, changes in daily variability were examined for the five models that were downscaled dynamically. The solid lines of Fig. 5 show probability density functions (PDFs) of baseline and future daily land-averaged temperatures generated through dynamical downscaling for January and July. The shape of future PDF is clearly very similar to that of the baseline for every GCM and for both months. In fact, the future PDF is nearly perfectly approximated by simply shifting the baseline PDF by the mean temperature difference (black dashed lines). This approximation holds equally well for the other 10 months (not shown). We took advantage of this finding to generate future PDFs for all statistically downscaled GCMs, starting with the baseline PDF and then shifting the mean by the temperature change given by the statistical model. To create the ensemble-mean future PDF, we started with the baseline PDF and shifted the mean by the ensemble-mean temperature change. All of the results in this section are based on this technique.

a. Daily average temperature distributions

Ensemble-mean land-averaged daily temperature distributions are shown for selected months corresponding to the four phases of the annual cycle in Figs. 6a–d. The most likely warming involves noticeable shifts of the temperature distribution toward higher values. The PDFs themselves are widest in the spring months, such as April, and narrowest in summer months, such as July. (This is consistent with the smaller levels in interannual variability in summer compared with spring seen in Fig. 4.)

To assess the degree to which daily average future temperatures will be similar to the baseline, we use a metric that quantifies how similar the current and future temperature distributions are: the fractional overlap between the two PDFs (an example shown in Fig. 6d).

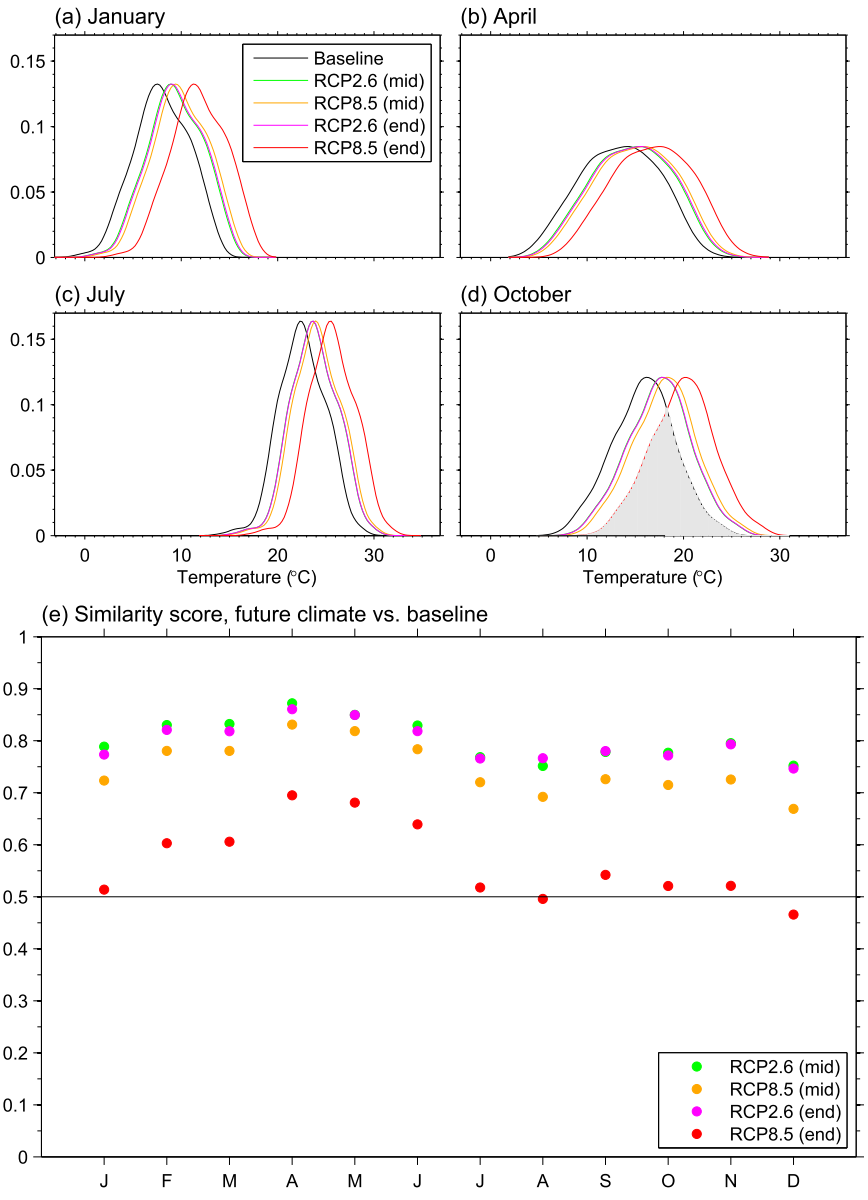

FIG. 6. PDFs of ensemble-mean, daily mean land-averaged surface air temperature (°C) during (a) January, (b) April, (c) July, and (d) October, representing each season in the baseline period (black) and at midcentury under RCP2.6 (green), midcentury under RCP8.5 (orange), end of century under RCP2.6 (magenta), and end of century under RCP8.5 (red). (e) Similarity score for each future scenario and time slice, defined as the percentage of area overlapping between future PDF and baseline PDF.

The interpretation of this similarity metric is the fraction of days in the future experiencing similar temperatures to the baseline period. The similarity metric is shown in Fig. 6e for each month and for both time slices and scenarios. In general, it is highest in the spring months and lowest in the late summer and early fall. This can be traced partly to the differences in variability between these two seasons noted above and also to the greater warming in late summer/early fall. Both of the time slices associated with the RCP2.6 emissions scenario give similarity scores of about 80%, indicating a pronounced but modest change in climate. The similarity scores for RCP8.5 midcentury are typically about 5% lower than those associated with the RCP2.6 cases. The RCP8.5 end-of-century case involves a dramatic reduction in the similarity scores, which hover around 45%–70%. Thus, under RCP8.5 only ½–⅔ of the end-of-century days will experience similar temperatures to

the baseline period. This is a strong indicator of a future climate state that is qualitatively different from the baseline.

b. Comparison of future and baseline percentiles

We also provide a complete mapping of the correspondences between baseline and future days. The percentile rank of each day in the baseline is paired with the percentile rank a day with the same temperature would have in a future period. Curves mapping these correspondences between percentiles of daily averaged temperature in the baseline (x axis) and future (y axis) for each time slice and scenario and for each calendar month are presented in Fig. 7. The corresponding percentiles in a future period to the baseline 50th percentile are shown at the intersections with the vertical lines. The $y = x$ gray lines show what the result would be if there were no changes in the distributions. For example, for July the 50th percentile in the baseline corresponds to the 7th percentile under RCP8.5 at end of century (intersection of red curve and vertical gray line). Therefore, 93% of future July days in this time slice and scenario will be warmer than the baseline median temperature. In the case of RCP2.6 at end of the century, 71% of future July days will be warmer than the baseline median temperature (intersection of magenta curve and vertical gray line), again indicating a noticeable but relatively smaller change in climate. Intersections of curves and horizontal lines show the corresponding baseline percentile to the 50th percentile temperature in a given future period under a certain scenario. For example, the 50th percentile for January under RCP8.5 at end of century corresponds to the 90th percentile in the baseline; while in the case of RCP2.6 at end of century the 50th percentile for January corresponds to the 66th percentile in the baseline. In general, the shape of each curve indicates the similarity of the future state to the baseline, with higher concavity corresponding to a more dramatic shift. The concavity is largest in RCP8.5 at end of century, with each percentile in the baseline typically corresponding to a future percentile that ranks tens of percentage points lower in the distribution. The concavity is least under RCP2.6, with RCP8.5 at midcentury being somewhat less similar to the baseline than the two RCP2.6 time slices.

c. Heat extremes

In this study, an extremely hot day is defined as one in which the daily maximum temperature (T_{max}) exceeds 35°C (95°F). See the appendix for how daily maximum surface air temperature is calculated in this case. Our dynamically downscaled simulation generates temperature snapshots every three hours, and we selected a 1600 local time (LT) snapshot because it is the closest to the time that the observed maximum temperature typically occurs. The model-calculated daily maximum temperatures from the baseline still validate well against a network of 21 weather stations (see the appendix). This gives us confidence that modeled extremely hot days correspond to actual hot days experienced throughout the region.

In the baseline period, most of the coastal and mountain areas have fewer than 10 extremely hot days per year (Fig. 8a). In contrast, inland regions such as the Mojave Desert, Coachella Valley, and Central Valley all contain areas exceeding 100 extremely hot days per year. While frequent extreme temperatures are mostly limited to inland regions, parts of the coastal zone have more than 60 extremely hot days per year. These regions are valleys that are somewhat removed from the moderating effects of the sea breeze, despite lying on the coastal side of the major mountain complexes. Strong gradients in the number of extremely hot days—such as those within the coastal zone—are an important reason to perform dynamical downscaling to such high resolution. With lower resolution, it could be difficult to distinguish important differences in extreme temperature behavior between these locations.

To quantify future extremely hot days, we started by examining the dynamically downscaled simulations. We found that the distributions of future daily maximum temperatures could be approximated almost perfectly by the baseline distribution shifted by the change in average temperature. (These results are not shown, but they are very similar to the daily mean results shown in Fig. 5.) Taking advantage of this finding, we created future distributions of daily maximum temperatures by shifting the baseline distributions by the temperature changes provided by the statistical model. These future distributions, generated based on the ensemble-mean warming, were used in the analysis that follows.

The number of extremely hot days increases most under the RCP8.5 scenario at end of century. With the exception of the highest elevations and a narrow swath very near the coast, where the increases are confined to a few days, land locations see 60–90 additional extremely hot days per year by the end of century (Fig. 8e). Thus, most land areas will effectively experience a new season of extreme heat. Downtown Los Angeles will see a rise from 6 to 54 extremely hot days, while at Riverside the number will roughly double, from 58 to 128 (Table 1). For midcentury under RCP8.5, and under RCP2.6 for both time slices, the spatial pattern is similar to RCP8.5 at end of century, but the increases are smaller. Most land areas see increases of roughly 20–40 additional extremely hot days per year. Downtown Los Angeles will experience a dozen or so more extremely hot days,

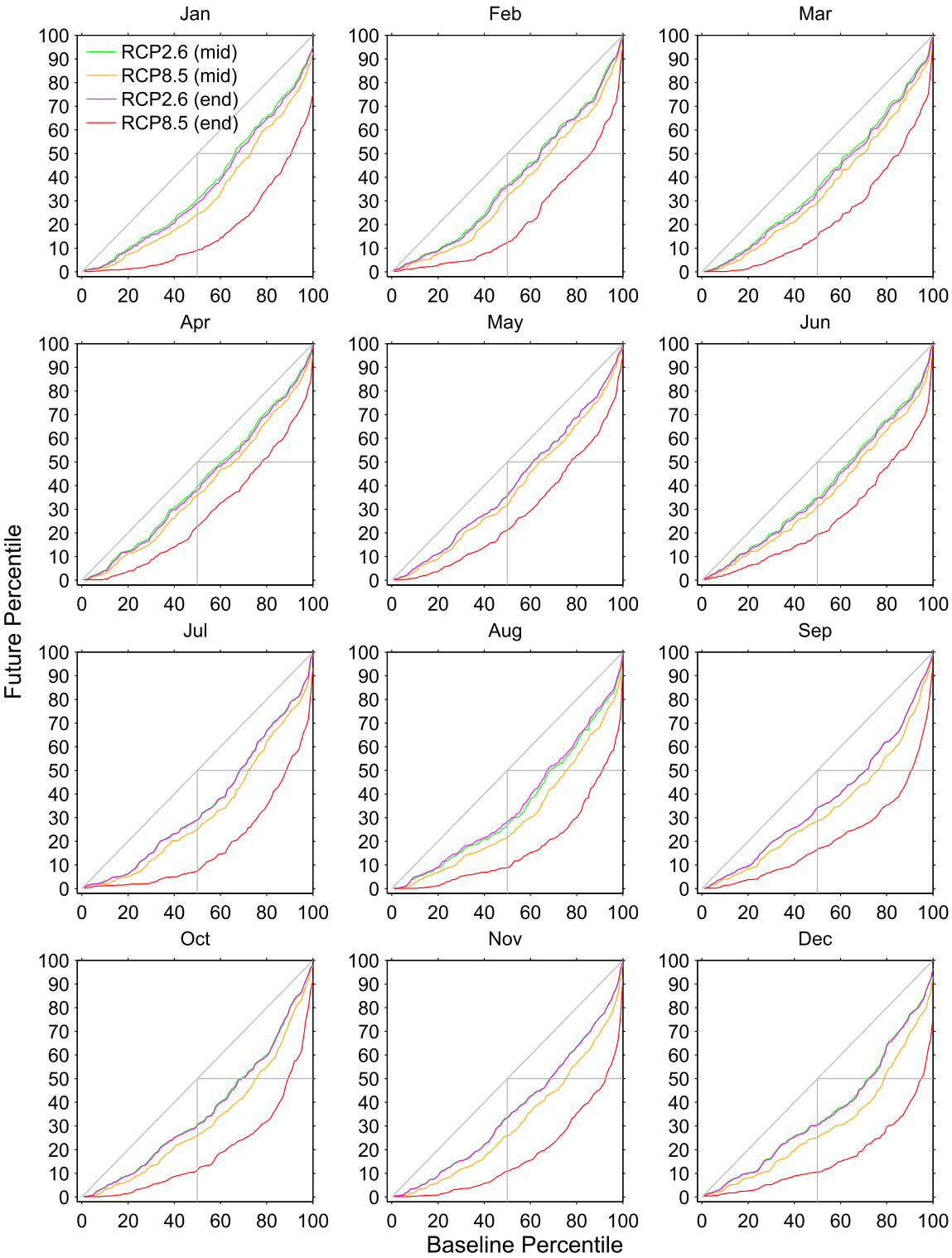

FIG. 7. Correspondence between percentiles of daily averaged temperature in the baseline (*x* axis) and future period (*y* axis) for each calendar month and for midcentury and end of century for RCP8.5 and RCP2.6 scenarios. The corresponding percentile in the future (baseline) to the baseline (future) 50th percentile is shown at the intersection with the vertical (horizontal) gray line.

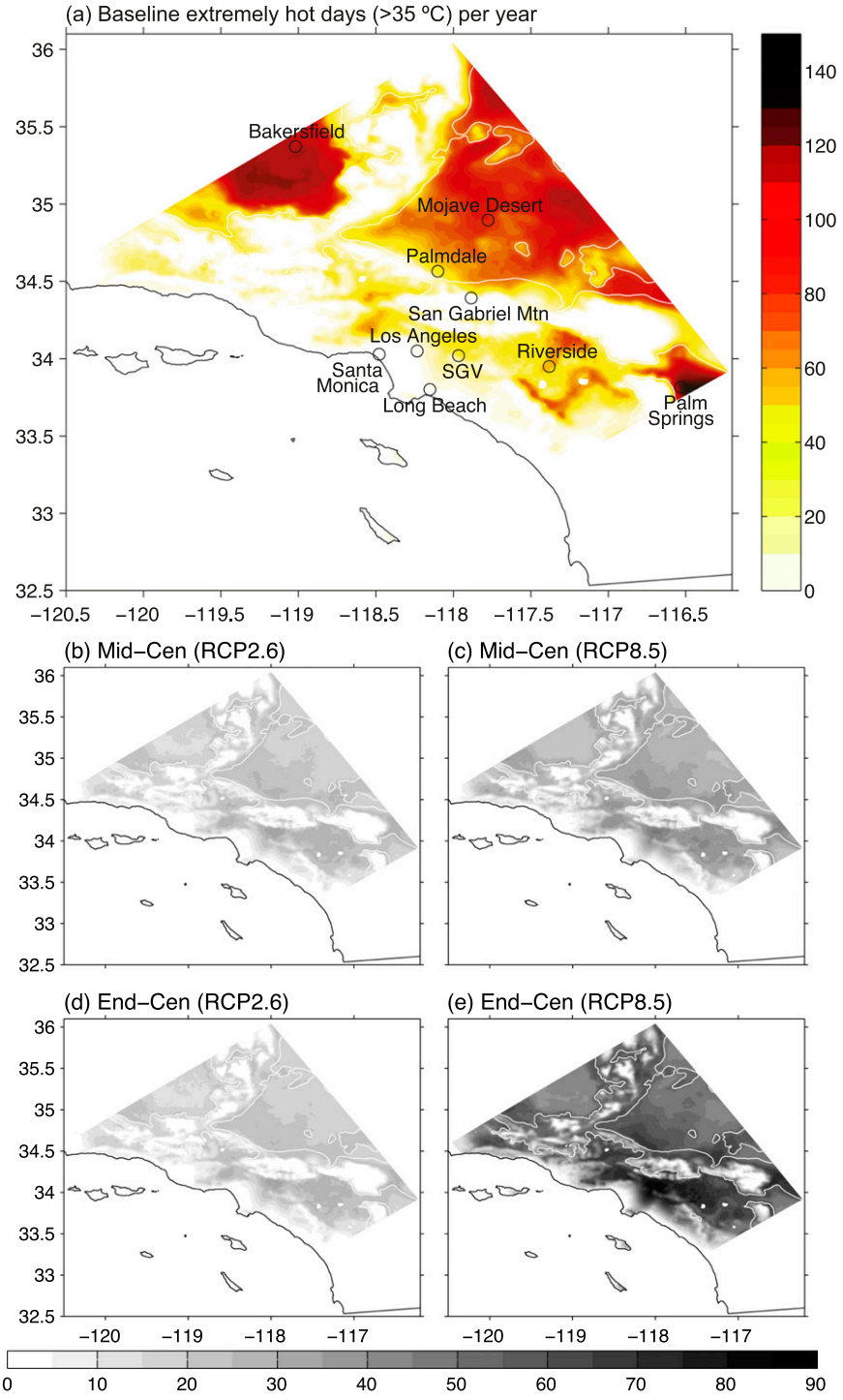

FIG. 8. (a) The number of extremely hot days per year ($T_{max} > 35$°C) for the baseline; and the change of number of extremely hot days per year for the (b) midcentury under RCP2.6, (c) midcentury under RCP8.5, (d) end of century under RCP2.6, and (e) end of century under RCP8.5. The 1000-m elevation contour is shown in white. SGV denotes the San Gabriel valley.

TABLE 1. Average number of extremely hot days (daily $T_{max} > 35°C$) per year for selected sites in the Los Angeles region. Results are shown for the baseline, midcentury, and end-of-century projections for both RCP8.5 and RCP2.6 emission scenarios.

	Baseline	RCP2.6 midcentury	RCP8.5 midcentury	RCP2.6 end of century	RCP8.5 end of century
Bakersfield	111	127	134	127	154
Long Beach	4	11	16	11	37
Los Angeles	6	16	22	15	54
Mojave Desert	90	110	120	109	141
Palm Springs	135	149	158	149	179
Palmdale	36	59	71	58	104
Riverside	58	86	98	86	128
San Gabriel valley	32	62	74	61	117
San Gabriel Mountain	0	0	1	0	8
Santa Monica	0	1	1	1	3

roughly a tripling, while Riverside will see approximately a 50% increase (Table 1). The highest elevations and locations very near the coast see almost no change in this quantity.

Although areas with more extremely hot days during the baseline period generally also see larger increases, the largest increase actually occurs in the San Gabriel valley, a part of the coastal zone. This phenomenon can be understood by examining the baseline and future distributions shown in Fig. 9. (Future distributions shown are for RCP8.5 at end of century.) At the San Gabriel valley location (Fig. 9a), where the largest increase in extremely hot days occurs (Fig. 8e), the peak in the baseline maximum temperature distribution occurs at about 32.5°C. Thus, a warming of 4°C pushes the peak of the distribution well past the 35°C threshold, resulting in nearly a quadrupling of the number of extremely hot days per year, from 32 in the baseline to 117 at the end of the century. In contrast, at a location in the Mojave Desert farther inland (Fig. 9c), the increase is smaller (from 90 to 141), even though the baseline number of extremely hot days is larger. Despite the fact that the warming is about 0.7°C (17%) larger here than in the coastal zone, the increase in extremely hot days is smaller because the baseline distribution is broader and its peak already lies above the 35°C threshold. In much cooler coastal locations closer to the ocean, such as Santa Monica (Fig. 9d), few baseline days are close to the threshold so that a warming of 4°C only results in an increase from 0 to 3 extremely hot days per year.

The generally greater warming in the interior could be a factor behind the larger increases in the numbers of extremely hot days in these locations. However, the results discussed above suggest that given an approximation of the overall warming in the region, the relationship between the baseline temperature distribution and the 35°C threshold may be more important in determining the increase in the number of extremely hot days at any particular location. A sensitivity test was performed to see if differences in warming throughout the domain were, in fact, important factors: The baseline distribution at each of our selected locations was shifted to reflect the same warming (Fig. 9, red dashed lines). In this case, we chose the warming that occurs at the coast. To assess the impact of spatial variations in the warming, the resulting number of future extremely hot days can be compared to the number that takes into account the local warming (Fig. 9, solid red lines). For the San Gabriel valley and Mojave Desert locations (Figs. 9a,c), the increase is nearly identical. A somewhat contrasting situation is seen in the San Gabriel Mountains (Fig. 9b), where a significant fraction (~50%) of the increase can be attributed to the enhanced warming occurring in the mountains. These findings suggest that even in this area of complex topography, there is only a modest benefit to dynamical downscaling in projecting future changes in extremely hot days. However, a credible downscaling approach is required to reproduce the baseline climate accurately.

d. Cold extremes

For the purposes of this study, we define an extremely cold day as one in which the daily minimum surface air temperature (T_{min}) drops below 0°C. This particular measure of cold extremes has significance to the hydrological cycle because surface air temperature relative to the freezing line is tightly linked to the partitioning between rain and snow during a precipitation event, the freezing and thawing of the snowpack, and frost formation. This measure of cold extremes also has ecological significance, since freezing temperatures can eliminate plant and animal pathogens (e.g., Chakraborty 2013; Raffa et al. 2013). Note that a blend of the surface skin temperature and 2-m temperature is used to calculate the surface air temperature (see the appendix).

In the baseline climate simulation, many parts of the region experience virtually no extremely cold days per year (Fig. 10a). However, extremely cold days occur frequently in the region's mountainous areas,

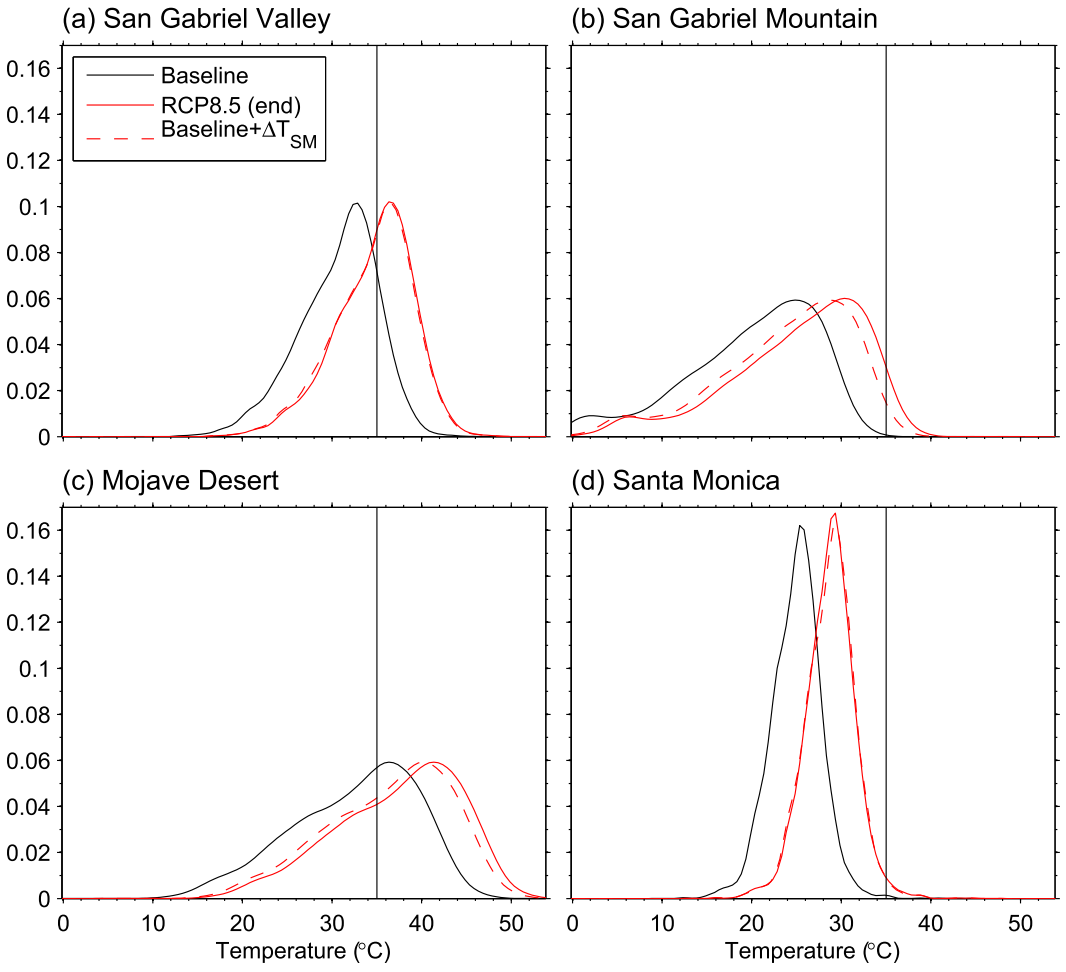

FIG. 9. PDFs of daily maximum temperature at selected sites during warm months (June–October) for baseline period (solid black), end of century under RCP8.5 (solid red), and baseline shifted by warming at Santa Monica location (dashed red). Vertical line indicates the 35°C threshold.

with some high-elevation locations experiencing as many as 200 days yr^{-1}. Here we focus on changes in the mountainous areas where freezing temperatures occur. Figures 10b–e show that in future time slices large reductions in cold days occur at high elevations. Under RCP8.5, end-of-century changes are especially dramatic, with some portions of the southern Sierra Nevada, San Gabriel Mountains, and San Bernardino Mountains seeing a decrease of roughly 50–90 days yr^{-1}. This represents nearly a full quarter of the year reduction in the number of days below freezing. In most cases, the reduction represents a majority of the baseline number. For example, at Big Bear Lake the number goes down from 142 to 55 days yr^{-1} and at Lake Arrowhead from 54 to 17 (Table 2). At Victorville and Palmdale, freezing temperatures practically disappear. The total area of the region experiencing at least 1 day per yr^{-1} with freezing temperatures decreases to less than half its value in the baseline. Under RCP2.6 for both time slices and under RCP8.5 midcentury, the reductions in the numbers of days per year are generally smaller, usually limited to 20–30 days (Fig. 10 and Table 2), and the total area of the region experiencing at least 1 day yr^{-1} with freezing temperatures decreases to roughly 80% of its value in the baseline.

Though both emissions scenarios and time slices show fewer extremely cold days overall, in none of these four future cases do extremely cold days disappear completely throughout the region. The future occurrence of weather events involving freezing temperatures in the greater Los Angeles region therefore cannot be interpreted as an absence of climate change.

4. Discussion and conclusions

Using a dynamical–statistical technique, we downscale temperature change relative to a baseline period (1981–2000) in the greater Los Angeles region for two

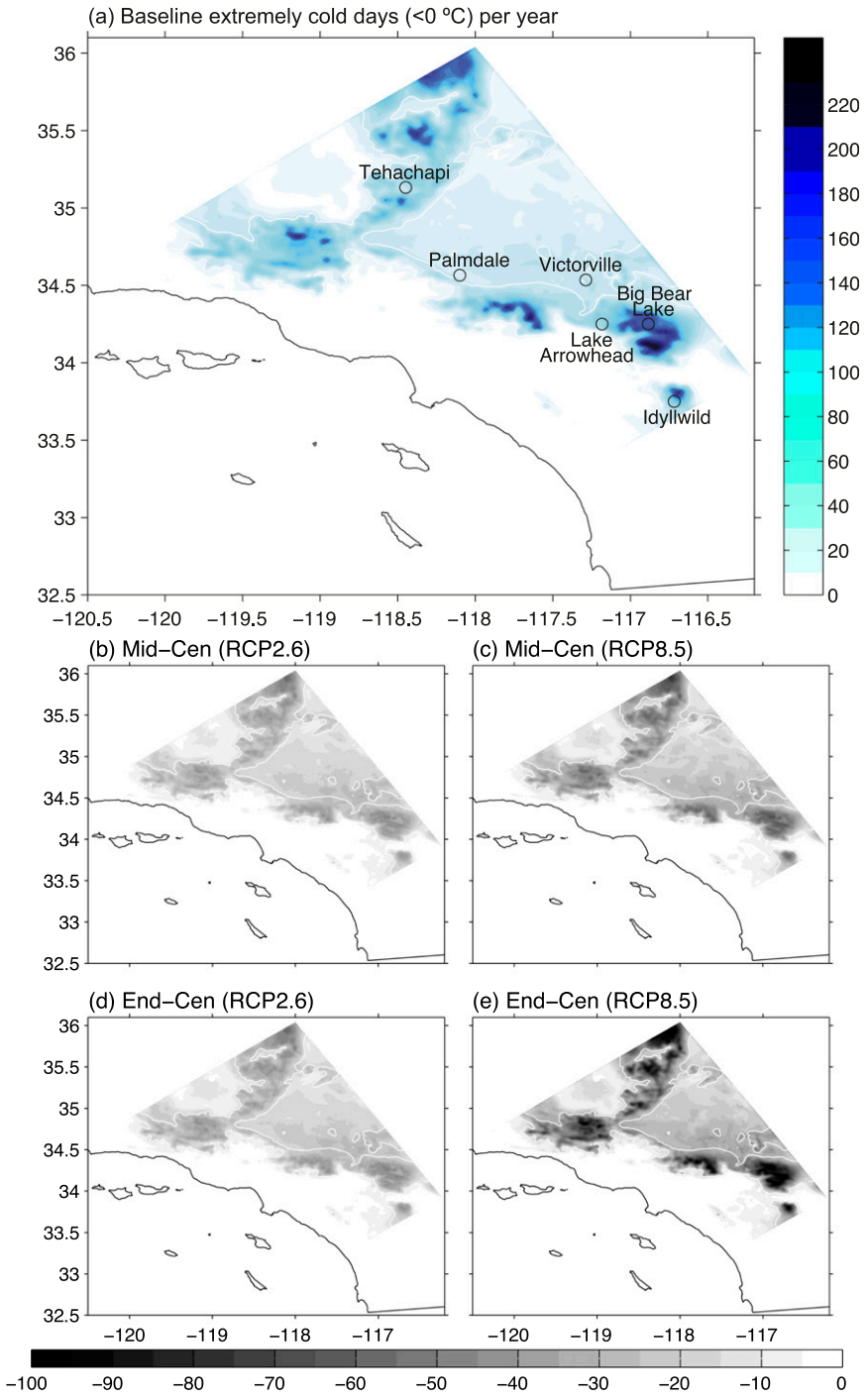

FIG. 10. (a) The number of extremely cold days per year ($T_{min} < 0$°C) for the baseline; and the change of number of extremely cold days per year for the (b) midcentury under RCP2.6, (c) midcentury under RCP8.5, (d) end of century under RCP2.6, and (e) end of century under RCP8.5. The 1000-m elevation contour is shown in white.

TABLE 2. Average number of extremely cold days (daily $T_{min} < 0°C$) per year for selected sites in the Los Angeles region. Results are shown for the baseline, midcentury, and end-of-century projections for both RCP8.5 and RCP2.6 emission scenarios.

	Baseline	RCP2.6 midcentury	RCP8.5 midcentury	RCP2.6 end of century	RCP8.5 end of century
Big Bear Lake	142	99	83	98	55
Idyllwild	77	47	38	46	21
Lake Arrowhead	54	34	28	33	17
Palmdale	26	8	4	7	1
Tehachapi	38	18	12	17	5
Victorville	44	15	9	15	2

future time slices: midcentury (2041–60) and end of century (2081–2100). We focus on two representative concentration pathways, corresponding to greenhouse gas emission reductions over coming decades (RCP2.6) and to continued twenty-first-century emission increases (RCP8.5). We downscale all available global climate models in the CMIP5 ensemble to provide likelihood and uncertainty estimates.

By the end of century under RCP8.5, a distinctly new regional climate state emerges against a background of considerable natural variability. This can be seen in more than one measure of change. First, average temperatures will almost certainly be outside the interannual variability range seen in the baseline. This statement is most applicable during the summer and fall, when the average future temperature in the model with the least warming is greater than even the very warmest year of the baseline. Second, the number of extremely hot days, defined as days when the daily maximum temperature exceeds 35°C, will increase significantly. Except for the highest elevations and a narrow swath very near the coast, land locations will likely see 60–90 additional extremely hot days per year, effectively adding an entirely new season of extreme heat. Third, days when minimum temperatures dip below freezing will decrease. In the baseline, there are typically dozens of days per year in mountainous areas when this occurs, but under RCP8.5 their number typically decreases by more than half. Finally, according to a similarity metric that quantifies the degree of correspondence between baseline and future distributions of daily temperature variability, the RCP8.5 end-of-century climate will most likely be only about 50% similar to the baseline.

Under RCP2.6 for midcentury and end-of-century time slices, these same measures indicate a climate shift that is less pronounced but still substantial. Future ensemble-mean average temperatures increase but lie just within the range of baseline interannual variability for all months except August. Therefore, future average monthly temperatures will likely be as warm as the hottest months in the baseline. Extremely hot days will occur more frequently, with roughly 20–40 additional extremely hot days per year over much of the land areas, though this is noticeably less than the 60–90 additional hot days experienced at the end of century under RCP8.5. Freezing days occur less frequently under RCP2.6 at midcentury and end of century, but again the reductions under RCP8.5 at end of century are twice as large. Similarity scores for the RCP2.6 scenario indicate that future daily temperatures will be roughly 80% similar to those experienced during the baseline period. Adaptation to this level of climate change should be easier, because future temperatures are mostly still within the envelope of variability to which human inhabitants and ecosystems are accustomed.

At midcentury, warming under RCP2.6 is nearly as large as that under RCP8.5, indicating that global emissions reductions would not prevent climate change in the region in the first half of the twenty-first century. At midcentury, warming under RCP2.6 is still 70% of the warming under RCP8.5. Similarity scores for the two cases are within roughly 5% of one another, and the changes in extremely hot and cold days are similar. Thus, some climatic changes would occur by midcentury regardless of choices regarding emission reductions. However, the impact of global emissions reductions becomes dramatic as the twenty-first century draws to a close. As we have detailed, they are necessary to prevent a dramatic shift in the regional climate state.

This downscaling approach used in this study allows us to quantify how the GCM climate change signals are expressed at the regional scale without the GCM future simulation being subject to the very large biases often found in the historical simulations of GCMs. A caveat of this work is that we only downscale the effects of a change in mean climate. In the dynamical downscaling experiments at the core of our methodology, we add the mean changes between future and baseline 20-yr climatologies for each calendar month to the baseline reanalysis boundary and initial conditions. Therefore, our simulations tell us how the baseline period would have been different if the monthly mean climatologies were altered to reflect the GCM climate change signals. This approach is independently developed and is similar to previously

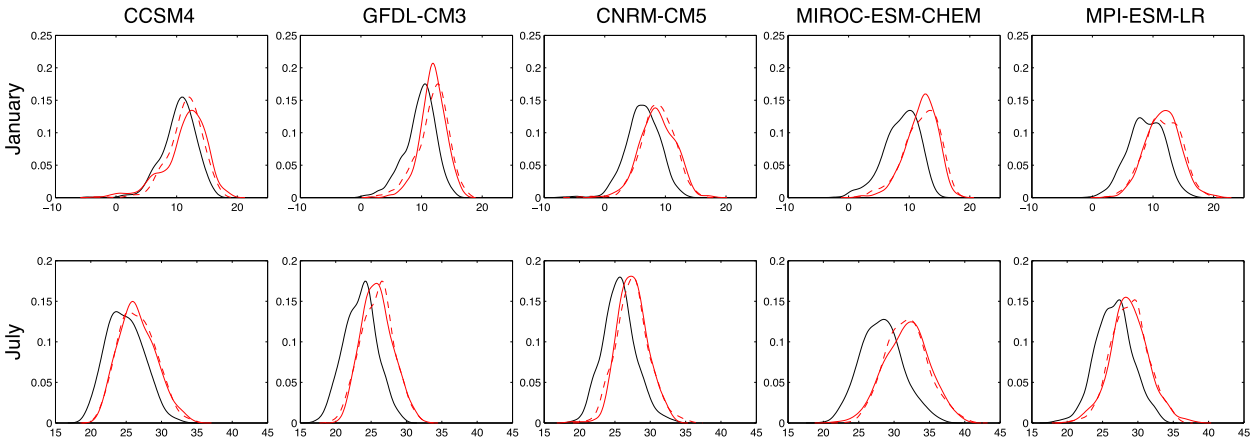

FIG. 11. PDFs of daily mean, area-mean (33°–36°N, 117°–120°W) surface air temperature in (top) January and (bottom) July during the baseline (black) and at midcentury under RCP8.5 emissions scenario (red) for five raw GCMs. The baseline distribution shifted by the mean temperature change (red dashed) for each GCM is shown for comparison.

developed procedures in recent regional climate downscaling studies (e.g., Schär et al. 1996; Hara et al. 2008; Knutson et al. 2008; Kawase et al. 2009; Lauer et al. 2010; Rasmussen et al. 2011; Seo and Xie 2011; Gutmann et al. 2012). It assumes that the weather and transient signals (e.g., frequency and intensity) applied on the model domain's boundaries remain structurally the same in the future simulation as in the baseline. Accordingly, we do not incorporate the changes in variability from daily to interannual scales in the boundary forcing (e.g., Knutson et al. 2008; Rasmussen et al. 2011). Therefore, the potential changes in GCM variability are not downscaled. This could be a limitation of our downscaling technique, especially when it comes to projecting changes in extremes.

One way to shed light on this issue is to investigate variability changes in the raw GCM output. We examine the daily PDF distributions within each calendar month for the five dynamically downscaled GCM projections for the baseline period and the midcentury period under RCP8.5 emissions scenario. Figure 11 compares the distribution of daily area-mean (33°–36°N, 117°–120°W) surface air temperature in January and July in the two periods. The solid lines show the distribution of baseline (black) and midcentury (red) separately. While the shapes of the distributions are not identical between baseline and midcentury for each GCM, they are very similar for both months. Therefore, the midcentury distribution for each month can be approximated by shifting the baseline distribution by the mean temperature change (red dashed lines). Examination of PDFs for the other calendar months reveals that this approximation still holds well (not shown). These results suggest that in the domain of interest (i.e., the Los Angeles region) the GCM-derived changes in daily temperature variability are rather small and secondary to the shift of the mean. It seems unlikely the weather activities would substantially change in GCMs from the baseline to future in the domain of interest. If these changes in GCM temperature variability were downscaled, it is likely that they would be equally subtle in the downscaled data. Therefore, we conclude the local changes in extremely hot and cold days projected in this study are reasonably accurate and are not subject to the limitation of the methodology.

Acknowledgments. Support for this work was provided by the City of Los Angeles and the U.S. Department of Energy as part of the American Recovery and Reinvestment Act of 2009. Additional funding was provided by the National Science Foundation (Grant EF-1065863, "Collaborative Research: Do Microenvironments Govern Macroecology?") and the Southwest Climate Science Center. The authors thank Dr. Dan Cayan for reviewing an early draft of this work and the two anonymous reviewers for their valuable comments.

APPENDIX

Improving Model Estimates of Extremes

When we used the dynamically downscaled 2-m air temperature output from the Weather Research and Forecasting Model, a regional model, the number of simulated extremely hot days ($T_{max} > 35$°C) during the baseline period was too low in comparison with observational point measurements (Table A1). Here we explain the potential causes of the underestimation and then come up with a new formula that better quantifies

TABLE A1. Average number of extremely hot days per year for 21 sites in the greater Los Angeles area. An extremely hot day is defined as a day in which the daily maximum surface air temperature is greater than 35°C (95°F). Results are shown for station observations, T_{2m}, and weighted average of modeled T_{2m} and TSK.

Station name	Observed	T_{2m}	$^1/_3T_{2m} + {}^2/_3$TSK
Palmdale	75 ± 8	10	47
Lancaster	56 ± 8	14	53
Palm Springs	148 ± 7	96	144
Van Nuys	35 ± 4	8	49
Downtown Los Angeles	10 ± 3	1	6
Bakersfield	69 ± 8	50	103
Long Beach	7 ± 2	1	6
Los Angeles International Airport (LAX)	2 ± 0.4	0	0
Big Bear Lake	0.1 ± 0.03	0	0.2
Riverside	60 ± 8	10	59
Burbank	27 ± 5	4	31
Pasadena	31 ± 6	3	29
Pomona	20 ± 5	4	30
Santa Barbara	1 ± 0.3	1	5
Oxnard	0.7 ± 0.2	0.2	0.1
Santa Ana	7 ± 2	1	5
Santa Monica pier	0.2 ± 0.03	0	0
Dry Canyon Reservoir	66 ± 7	8	37
San Bernardino	59 ± 8	22	83
Torrance	2 ± 0.8	0.2	1
Redlands	61 ± 8	19	68

number of the extremely hot days. This new formula also improves estimates for extremely cold days.

The observational dataset used is a set of quality-controlled, daily maximum near-surface temperature observations taken during the baseline period (1981–2000) from 21 weather stations. These data were obtained from the National Climatic Data Center (NCDC; http://www.ncdc.noaa.gov/oa/ncdc/html). Unlike this observational dataset, where the temperatures were recorded every 10 min, in our simulations, we only saved a snapshot of the air temperature output every 3 h (at 1000, 1300, 1600, 1900 LT, etc.) Since the temperature is not recorded at the exact time the true daily maximum (minimum) is achieved, our modeled maximum (minimum) temperatures will be an underestimation (overestimation) of what WRF actually produced. This leads to an underestimation (overestimation) of the number of extremely hot (cold) days.

Another source of discrepancy may come from the height at which the temperature measurements are taken. To measure surface air temperature in WRF, we use the air temperature at a reference height of 2 m. While WRF interpolates the temperature to two meters height from the temperature of its atmospheric layer closest to the surface, the thermometer at the weather stations is set between 1 and 2 m above the ground. Because the ground is the source of heat during the day, the closer the thermometer is to the ground, the warmer the observed temperature. Therefore, the mismatch between the modeled reference height and true observed height may partially account for the model's bias of the observed surface air temperature. The particular technique used by WRF to interpolate 2-m temperatures from the temperature of the surface layer may also lead to a bias, compared with the observed surface air temperature.

To better diagnose the simulated extremes in the baseline simulation and the future changes, we developed a formula to describe the daily maximum surface air temperature more realistically. We tested a series of different combinations of model-simulated surface skin temperature (TSK) and 2-m air temperature (T_{2m}) and found that a combination of two-thirds TSK and one-third T_{2m} gives the most realistic estimation (smallest root-mean-square error) of the observed extremes (Fig. A1). The daily maximum surface air temperature is taken to be this blend of surface and surface air temperatures, taken at 1600 LT. This new method validates well against the point measurements in the observational network and provides a significant improvement over using T_{2m} alone (Table A1). For example, for the city of Lancaster, the new method produces 53 extremely hot days per year, while the observed number of extremely hot days is 56 ± 8 days yr^{-1}, a significant improvement over the 14 days yr^{-1} predicted by T_{2m} alone. Because of these improvements, this method is used for the calculations of extremely hot days.

The particular blend of two-thirds surface skin temperature plus one-third 2-m temperature was also found to produce the best results for modeling daily minimum

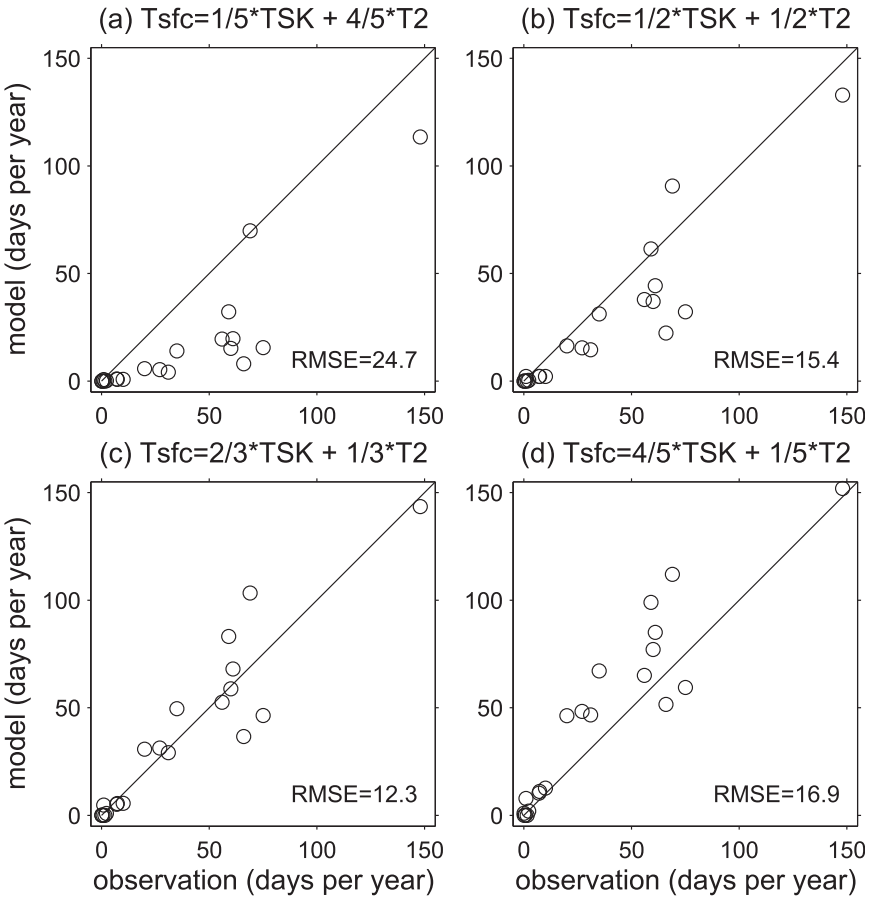

FIG. A1. Scatterplots of the numbers of extremely hot days from the observations and the dynamically downscaled simulations. Each panel presents the results based on a matrix blending TSK and T_{2m} with different weighting. The root-mean-square error (RMSE) for each matrix is denoted.

surface air temperatures (not shown). As with the maximum temperature, the minimum temperature can occur at any time. The closest time to the average observed minimum when a WRF snapshot is taken is 0400 LT. Thus, daily minimum temperatures are calculated as a weighted average of 2-m and surface skin temperatures at 0400 LT.

REFERENCES

Abatzoglou, J. T., K. T. Redmond, and L. M. Edwards, 2009: Classification of regional climate variability in the state of California. *J. Appl. Meteor. Climatol.,* **48,** 1527–1541, doi:10.1175/2009JAMC2062.1.

Bindoff, N. L., and Coauthors, 2013: Detection and attribution of climate change: From global to regional. *Climate Change 2013: The Physical Science Basis,* T. F. Stocker et al., Eds., Cambridge University Press, 867–952. [Available online at http://www.ipcc.ch/pdf/assessment-report/ar5/wg1/WG1AR5_Chapter10_FINAL.pdf.]

Cabré, M., S. A. Solman, and M. N. Nuñez, 2010: Creating regional climate change scenarios over southern South America for the 2020's and 2050's using the pattern scaling technique: Validity and limitations. *Climatic Change,* **98,** 449–469, doi:10.1007/s10584-009-9737-5.

Cayan, D. R., E. P. Maurer, M. D. Dettinger, M. Tyree, and K. Hayhoe, 2008: Climate change scenarios for the California region. *Climatic Change,* **87** (Suppl 1), 21–42, doi:10.1007/s10584-007-9377-6.

Chakraborty, S., 2013: Migrate or evolve: Options for plant pathogens under climate change. *Global Change Biol.,* **19,** 1985–2000, doi:10.1111/gcb.12205.

Déqué, M., and Coauthors, 2007: An intercomparison of regional climate simulations for Europe: Assessing uncertainties in model projections. *Climatic Change,* **81,** 53–70, doi:10.1007/s10584-006-9228-x.

Deser, C., R. Knutti, S. Solomon, and A. S. Phillips, 2012a: Communication of the role of natural variability in future North American climate. *Nat. Climate Change,* **2,** 775–779, doi:10.1038/nclimate1562.

——, A. Phillips, V. Bourdette, and H. Teng, 2012b: Uncertainty in climate change projections: The role of internal variability. *Climate Dyn.,* **38,** 527–546, doi:10.1007/s00382-010-0977-x.

——, ——, M. Alexander, and B. Smoliak, 2013: Projecting North American climate over the next 50 years: Uncertainty due to

internal variability. *J. Climate,* **27,** 2271–2296, doi:10.1175/JCLI-D-13-00451.1.

Duffy, P. B., and Coauthors, 2006: Simulations of present and future climates in the western United States with four nested regional climate models. *J. Climate,* **19,** 873–895, doi:10.1175/JCLI3669.1.

Gutmann, E., R. Rasmussen, C. Liu, D. J. Gochis, and M. Clark, 2012: A comparison of statistical and dynamical downscaling of winter precipitation over complex terrain. *J. Climate,* **25,** 262–281, doi:10.1175/2011JCLI4109.1.

Hara, M., T. Yoshikane, H. Kawase, and F. Kimura, 2008: Estimation of the impact of global warming on snow depth in Japan by the pseudo-global-warming method. *Hydrol. Res. Lett.,* **2,** 61–64, doi:10.3178/hrl.2.61.

Hayhoe, K., and Coauthors, 2004: Emissions pathways, climate change, and impacts on California. *Proc. Natl. Acad. Sci. USA,* **101,** 12 422–12 427, doi:10.1073/pnas.0404500101.

Kawase, H., T. Yoshikane, M. Hara, F. Kimura, T. Yasunari, B. Ailikun, H. Ueda, and T. Inoue, 2009: Intermodel variability of future changes in the Baiu rainband estimated by the pseudo global warming downscaling method. *J. Geophys. Res.,* **114,** D24110, doi:10.1029/2009JD011803.

Knutson, T. R., J. J. Sirutis, S. T. Garner, G. A. Vecchi, and I. M. Held, 2008: Simulated reduction in Atlantic hurricane frequency under twenty-first-century warming conditions. *Nat. Geosci.,* **1,** 359–364, doi:10.1038/ngeo202.

Lauer, A., K. Hamilton, Y. Wang, V. T. J. Phillips, and R. Bennartz, 2010: The impact of global warming on marine boundary layer clouds over the eastern Pacific—A regional model study. *J. Climate,* **23,** 5844–5863, doi:10.1175/2010JCLI3666.1.

Meinshausen, M., and Coauthors, 2011: The RCP greenhouse gas concentrations and their extension from 1765 to 2300. *Climatic Change,* **109,** 213–241, doi:10.1007/s10584-011-0156-z.

Moss, R., and Coauthors, 2008: Towards new scenarios for analysis of emissions, climate change, impacts, and response strategies. IPCC Expert Meeting Rep., 155 pp.

Raffa, K. F., E. N. Powell, and P. A. Townsend, 2013: Temperature-driven range expansion of an irruptive insect heightened by weakly coevolved plant defenses. *Proc. Natl. Acad. Sci. USA,* **110,** 2193–2198, doi:10.1073/pnas.1216666110.

Rasmussen, R., and Coauthors, 2011: High-resolution coupled climate runoff simulations of seasonal snowfall over Colorado: A process study of current and warmer climate. *J. Climate,* **24,** 3015–3048, doi:10.1175/2010JCLI3985.1.

Salathé, E. P., L. R. Leung, Y. Qian, and Y. Zhang, 2010: Regional climate model projections for the state of Washington. *Climatic Change,* **102,** 51–75, doi:10.1007/s10584-010-9849-y.

Sato, T., F. Kimura, and A. Kitoh, 2007: Projection of global warming onto regional precipitation over Mongolia using a regional climate model. *J. Hyrdol.,* **333,** 144–154, doi:10.1016/j.jhydrol.2006.07.023.

Schär, C., C. Frei, D. Lüthi, and H. C. Davies, 1996: Surrogate climate-change scenarios for regional climate models. *Geophys. Res. Lett.,* **23,** 669–672, doi:10.1029/96GL00265.

Seo, H., and S.-P. Xie, 2011: Response and impact of equatorial ocean dynamics and tropical instability waves in the tropical Atlantic under global warming: A regional coupled downscaling study. *J. Geophys. Res.,* **116,** C03026, doi:10.1029/2010JC006670.

Stocker, T. F., and Coauthors, 2013: *Climate Change 2013: The Physical Science Basis.* Cambridge University Press, 1535 pp. [Available online at http://www.ipcc.ch/pdf/assessment-report/ar5/wg1/WG1AR5_ALL_FINAL.pdf.]

Taylor, K. E., R. J. Stouffer, and G. A. Meehl, 2012: An overview of CMIP5 and the experiment design. *Bull. Amer. Meteor. Soc.,* **93,** 485–498, doi:10.1175/BAMS-D-11-00094.1.

Wallace, J. M., C. Deser, B. V. Smoliak, and A. S. Phillips, 2015: Attribution of climate change in the presence of internal variability. *Climate Change: Multidecadal and Beyond,* C. P. Chang et al., Eds., World Scientific Series on Asia–Pacific Weather and Climate, Vol. 6., World Scientific, in press.

Walton, D. B., F. Sun, A. Hall, and S. Capps, 2015: A hybrid dynamical–statistical downscaling technique. Part I: Development and validation of the technique. *J. Climate,* **28,** 4597–4617, doi:10.1175/JCLI-D-14-00196.1.

Wilkinson, R., and T. Rounds, 1998: Climate change and variability in California: White paper for the California regional assessment. National Center for Ecological Analysis and Synthesis Research Paper 4, 67 pp. [Available online at https://www.nceas.ucsb.edu/ca/climate.pdf.]